Composites Part B 197 (2020) 108135

Contents lists available at ScienceDirect

Composites Part B

journal homepage: www.elsevier.com/locate/compositesb

Effects of sand filling on the dynamic response of corrugated core sandwich beams under foam projectile impact

Run-Pei Yu [a,b,c], Xin Wang [a,b,c], Qian-Cheng Zhang [a,b,d,*], Lang Li [a,b,c], Si-Yuan He [e], Bin Han [f], Chang-Ye Ni [c,g], Zhen-Yu Zhao [c,g], Tian Jian Lu [c,g,**]

[a] State Key Laboratory for Strength and Vibration of Mechanical Structures, Xi'an Jiaotong University, Xi'an 710049, PR China
[b] MOE Key Laboratory for Multifunctional Materials and Structures, Xi'an Jiaotong University, Xi'an 710049, PR China
[c] State Key Laboratory of Mechanics and Control of Mechanical Structures, Nanjing University of Aeronautics and Astronautics, Nanjing 210016, PR China
[d] Key Laboratory of Intense Dynamic Loading and Effect, Northwest Institute of Nuclear Technology, Xi'an 710024, PR China
[e] School of Biological Science & Medical Engineering, Southeast University, Nanjing 210016, PR China
[f] School of Mechanical Engineering, Xi'an Jiaotong University, Xi'an 710049, PR China
[g] Nanjing Center for Multifunctional Lightweight Materials and Structures, Nanjing University of Aeronautics and Astronautics, Nanjing 210016, PR China

ARTICLE INFO

Keywords:
Impact loading
Protective sandwich structure
Corrugated member
Sand-structure coupling

ABSTRACT

How sand filling affects the dynamic response of metallic corrugated sandwich beams under shock loading was characterized, both experimentally and numerically, with shock loading simulated by high-speed impact of aluminum foam projectiles at beam mid-span. To facilitate evaluating the effects of sand filling, both empty and sand-filled corrugated core sandwich beams were assessed and compared for shock resistance. Representative deformation processes, deformation and failure modes, and beam deflections were experimentally obtained and analyzed. Sand-filled sandwich beams exhibited much higher shock resistance than the empty ones. Numerical simulations were subsequently conducted using a coupled discrete particle/finite element approach that takes into account the coupling interaction between the sand grains and corrugation members. The simulations predicted reasonably well the primary features (permanent mid-span deflections and deformation modes) of both the empty and sand-filled sandwich beams observed experimentally. The validated numerical model was employed to evaluate how the properties of the filling sand and other granular filling materials, e.g., density, stiffness, friction and damping, affect the shock resistance of sandwich beams. The results indicated that the shock resistance was sensitive to, firstly, the density and stiffness of sand and, secondly, the friction between sand particles. In contrast, the damping between sand particles had little effect.

1. Introduction

Whereas extreme dynamic impact and blast loads greatly threaten the security of structural systems and their occupants, conventional commercial and private buildings are often designed not to withstand such impact and blast loadings, and it is inconvenient and expensive to strengthen existing building structures with permanent protective constructions. One of the solutions is using maneuverable prefabricated structures to shield buildings and other structures against extreme loads [1–5]. Such protective structures should not only be able to resist a variety of impact/blast threats, but also are easy to transport and install, preferably with modular designs. When extreme events happen, the maneuverable, quickly installed temporary protective structures can act as barriers to shield schools, hospitals, embassies and other vital facilities.

Sandwich panels with stiff, strong face sheets and high porosity cellular cores are ultralightweight and can dissipate a considerable amount of impact energy via large plastic deformation of the core and face sheets, thus attractive for constructing maneuverable temporary structures. A variety of core topologies including foams [6–9], honeycombs [10–13], folded plates (corrugations) [14–18] and pyramidal trusses [19–21] have been selected as the core of sandwich panels to

* Corresponding author. State Key Laboratory for Strength and Vibration of Mechanical Structures, Xi'an Jiaotong University, Xi'an, 710049, PR China.
** Corresponding author. State Key Laboratory of Mechanics and Control of Mechanical Structures, Nanjing University of Aeronautics and Astronautics, Nanjing, 210016, PR China.
E-mail addresses: zqc111999@xjtu.edu.cn, zqc111999@mail.xjtu.edu.cn (Q.-C. Zhang), tjlu@nuaa.edu.cn (T.J. Lu).

https://doi.org/10.1016/j.compositesb.2020.108135
Received 26 December 2019; Received in revised form 2 May 2020; Accepted 5 May 2020
Available online 18 May 2020

resist impact/blast loading. In particular, corrugated core sandwich structures stand out due to outstanding anti-impact performance [22] and relatively simple and efficient techniques needed for fabrication, e.g., extrusion [23] and laser welding [16]. The dynamic response of a sandwich panel with corrugated core subjected to foam projectile impact [14] and air blast loading [15,16] exhibited a higher shock resistance than its monolithic counterpart having equal mass.

Recently, to further improve the impact/blast resistance of sandwich structures with lattice truss cores, the concept of hybrid core design has been proposed wherein the interstices of the lattice truss core (e.g., corrugated plates) are filled with foam or other materials. Typically, with PVC foam selected as the filling material, corrugated sandwich panels exhibited improved performance under shock tube impulse and air blast loading [24,25], whereas superior penetration resistance was achieved by inserting ceramic prisms into a corrugated core sandwich panel [26]. Further, shear thickening fluid was used as the filler to improve the dynamic energy absorption capacity of sandwich structures [27]. The main aim of this study is to investigate the feasibility of using sand as a filling material for sandwich constructions with enhanced blast resistance, particularly for large-scale applications requiring quick assembling and low cost.

Sand as a readily available, low-cost granular material has been shown effective in mitigating blast shock wave [28–31]. The shock wave energy is dissipated during wave-sand interaction, as: (I) particle collision, friction and crushing through sand compaction will consume much energy; (II) high pressure gas filtration by sand attenuates the transmitted air shock wave; (III) if sand is not confined, the wave energy is partly transferred to the motion of sand particles. Sand barriers, e.g., sandbags [30] and sand-filled anti-blast walls [32,33], have therefore been widely used to shield against blast/shock effect. In recent years, sand-filled sandwich constructions as temporary protective structures have been envisioned. The filled sand can be emptied from the sandwich core with ease so that the system retains its ultralightweight for quick transportation and fast assembly. For instance, extruded aluminum corrugated sandwich panels filled with sand (and small rocks) have been proposed as mobile shelters with modular design for ISO containers [2,3]. Sand-filled fiber-reinforced polymer (FRP) composite sandwich panels were also investigated experimentally under blast and fragmentation loading, and the effects of panel thickness and inner core configuration were quantified [1]. At present, however, the dynamic response and sand-structure interaction of sand-filled metallic sandwich structures under shock loading are seldom studied, and how sand properties (e.g., density, grain size, surface texture and mineralogy [34]) affect the shock resistance remains elusive.

A combined experimental and numerical approach was used to characterize the dynamic response of sand-filled metallic corrugated core sandwich beams under shock loading, with the shock loading simulated using closed-cell aluminum foam projectiles [35]. A coupled discrete particle/finite element simulation scheme was proposed for numerical calculations, which was validated against experimental measurements. The validated numerical model was employed to systematically evaluate the effects of sand properties on shock resistance.

2. Experimental procedures

2.1. Specimen configuration and fabrication

With reference to Fig. 1, corrugated core sandwich beams used in the current study were comprised of two thin stainless steel faceplates, a stainless steel core with trapezoidal corrugation, and two low carbon steel block fixtures. Relevant geometric parameters included: sandwich beam span L and width W, face sheet thickness t_f, horizontal core segment width B_p, core height H_c, core web thickness t_c, inclination angle θ, steel block length L_b, and bolt hole diameter d_b. In the absence of filled sand, the empty corrugated core had a relative density of:

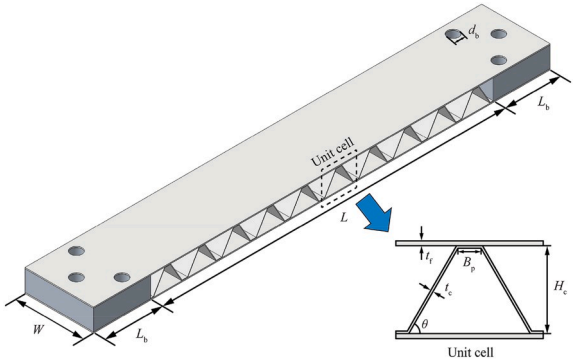

Fig. 1. Schematic illustration of corrugated core sandwich beam and its end fixture.

$$\overline{\rho}_c = \frac{B_p \sin\theta + H_c - t_c}{B_p \sin\theta + (H_c - t_c)\cos\theta} \frac{t_c}{H_c} \quad (1)$$

Values of the foregoing geometric parameters were summarized in Table 1.

Fig. 2 displayed the fabrication processes of empty corrugated core sandwich beams and sand-filled sandwich beams. Trapezoidal corrugated cores were manufactured by folding AISI 304 stainless steel sheets of width $W = 60$ mm and subsequently cut by electro-discharge machining to the length $L = 300$ mm. Then the 304 stainless steel face sheets and low carbon steel blocks (end fixtures; Fig. 1) supplied by Haocheng Co., Ltd. (Shanghai, China) were assembled together with the corrugated core. Note that, in order to achieve a fully clamped boundary condition, inserting the metal blocks enabled the sandwich core achieve full-densification between the fixtures under impact loading. Three holes with a diameter of $d_b = 10$ mm were prefabricated on each steel block and each end of face sheets so that the end portions of the sandwich beam could be bolted onto the support later. Subsequently, the face sheets, the corrugated core and the steel blocks were vacuum brazed together with Ni–Cr14–P10 (wt.%) braze alloy at the brazing temperature of 1040 °C and vacuum atmosphere of 5×10^{-3} Pa. The welded specimens were empty sandwich beams used in the experiments. Finally, the interstices of the corrugated core were fully filled with dry quartz sand through a funnel to form the sand-filled, hybrid-cored sandwich beams. The two open sides of the beams were sealed using strong and transparent rubberized tapes of thickness 0.7 mm to prevent the sand from premature leaking out during impact testing.

2.2. Material characterization

Cylindrical impact projectiles made from closed-cell aluminum foam were provided by Southeast University (Nanjing, China). Quasi-static compression tests were performed at a strain rate of 1×10^{-3} s^{-1} on cylindrical foam specimens with a diameter of 25 mm and a length of 50 mm. Typical uniaxial compressive response of the foam (relative density $\overline{\rho}_f \approx 0.14$) was presented in Fig. 3a, showing a plateau strength of approximately 4.5 MPa and a nominal densification strain of $\varepsilon_D \approx 0.6$. The measured compressive stress versus strain curve of the foam projectile was employed as input to subsequent numerical simulations. Note that relative density has great influence on the mechanical properties of the foam, so only projectiles with a relative density varying strictly in the range of 13%–15% were selected for carrying out the impact

Table 1
Geometric parameters of corrugated core sandwich beams (unit: mm).

L	W	t_f	B_p	H_c	t_c	$\theta/^\circ$	L_b	d_b	$\overline{\rho}_c/\%$
300	60	1	5	17.8	0.5	60	50	10	4.7

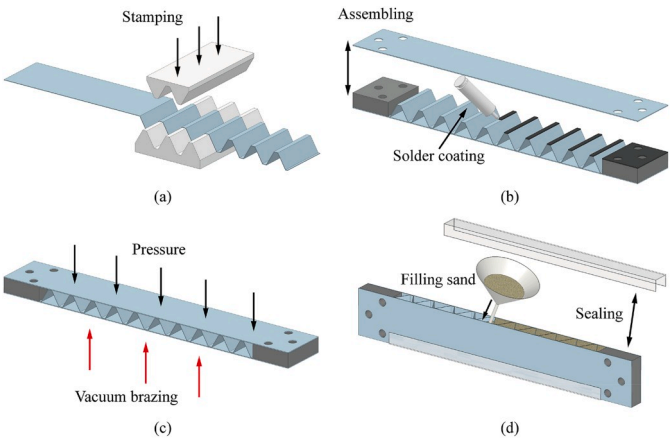

Fig. 2. Fabrication processes of sandwich beam specimens: (a) stamping, (b) assembling, (c) vacuum brazing, and (d) sand filling and sealing.

experiments.

Standard dog-bone tensile specimens were cut from as-received AISI 304 stainless steel sheets and then subjected to the same heating and cooling cycle for furnace brazing. Uniaxial tensile response of the 304 stainless steel (density of $\rho_s = 7800\ \ kg/m^3$) was measured at a nominal strain rate of $3.3 \times 10^{-3}\ \ s^{-1}$, and the true stress versus true strain curve was plotted in Fig. 3b. The material had a Young's modulus of $E_s = 200\ \ GPa$, yield strength of $\sigma_y = 180\ \ MPa$, and tangent modulus of $E_t = 2\ \ GPa$.

Quasi-static tensile tests were carried out at a strain rate of $6.7 \times 10^{-3}\ \ s^{-1}$ to determine the mechanical properties of the sealing tape used in the current study. Dimensions of the tensile specimen shown in Fig. 3c were designated by following the Standard Test Method for Tensile Properties of Thin Plastic Sheeting (ASTM D882-12). The nominal stress versus strain curve of the tape material plotted in Fig. 3c was calculated from the force and displacement data recorded by the MTS machine.

The quartz sand used as the filler material consisted of more than 98% silica and a small fraction of other elements (Fe_2O_3, Al_2O_3, etc.). The density of solid silica was 2650 kg/m^3 while the measured density of the sand compacted in the interstices of corrugated core was $1334 \pm 20\ \ kg/m^3$, implying an initial porosity of $49.7 \pm 0.8\%$. An optical micrograph was used to examine the sand grains as shown in Fig. 4a. The sand grains exhibited angular shape in the size range of 0.4–1.7 mm. Detailed size distribution curves were plotted in Fig. 4b, from which the median mass diameter (d_{50}) of the particles was found to be 0.9 mm. In addition, constrained compression tests were conducted to provide insight into the stress-strain response of the sand, which was employed later to calibrate the contacting parameters of discrete sand particles in the numerical simulation model. For constrained compression testing, sand particles were gently poured into a steel container to form a sand column of diameter 50 mm and initial height 20 mm. The initial porosity of the sand column was kept ~50%, same as that applied in the impact test. The sand was compressed with an MTS machine with a capacity of 250 kN and a least count of 0.1 kN. Due to the limit of the test apparatus, a small compressive load of 0.1 kN (corresponding to a pressure of 0.05 MPa) was firstly applied on the sand column via a steel punch, and the force and displacement recorded by MTS were zeroed (in line with Hagerty et al. [36]). Compressive load was then applied with a fixed strain rate of $1 \times 10^{-3}\ \ s^{-1}$, and the corresponding nominal stress versus strain response was calculated from the recorded force and displacement histories, as plotted in Fig. 3d.

2.3. Experimental setup

The impact test system consisted of a one-stage light gas gun, a clamping device and a high speed camera, as shown in Fig. 5. The gas

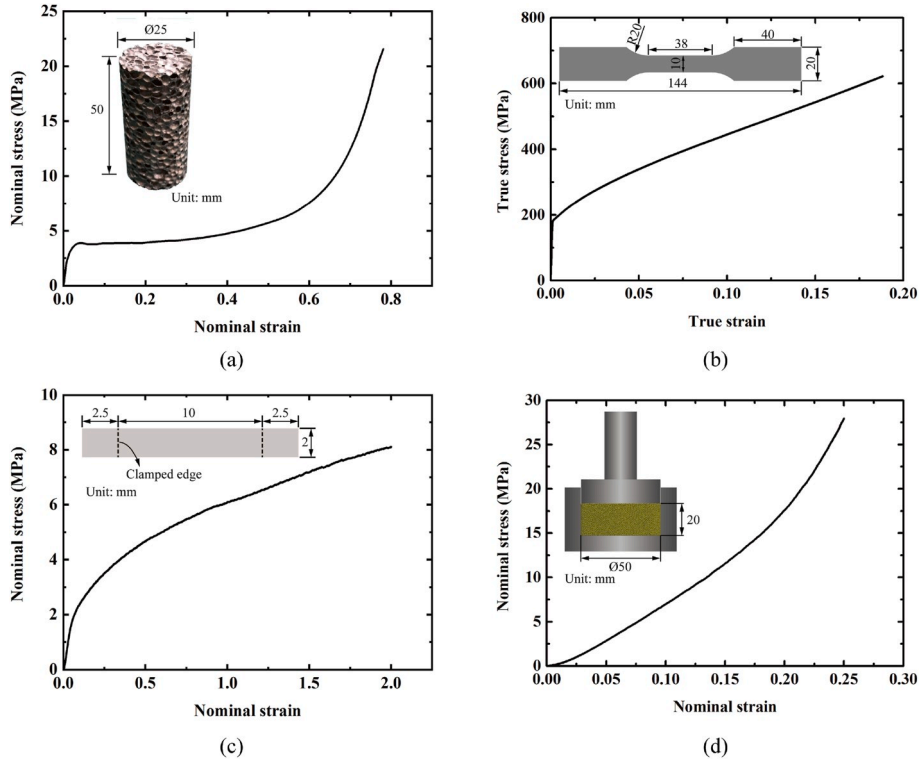

Fig. 3. Measured stress versus strain responses of constituent materials: (a) quasi-static nominal compressive stress versus strain response of aluminum foam, (b) quasi-static tensile response of 304 stainless steel after brazing cycle, (c) quasi-static nominal tensile stress versus strain response of sealing tape, and (d) quasi-static compression response of quartz sand in a constrained cylinder.

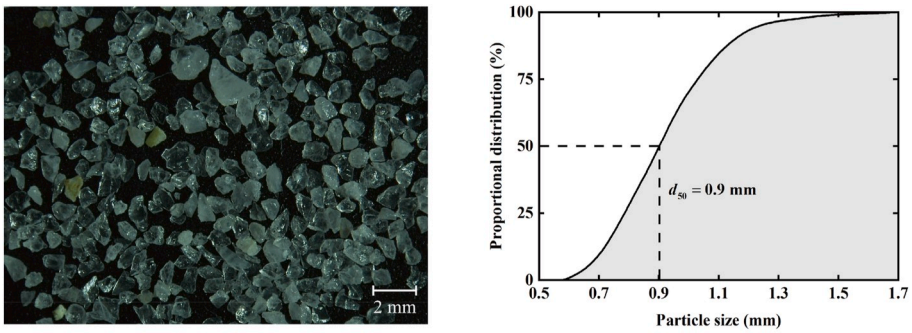

Fig. 4. (a) Magnified view of sand grains, and (b) particle size distribution of quartz sand.

gun with a barrel length of 5 m and an inner diameter of 57 mm used nitrogen gas at a prescribed pressure to launch aluminum foam projectiles. The foam projectiles provided impact loading on the mid-span of the clamped sandwich beam, enabling its dynamic response to be measured. The cylindrical foam projectiles had length $l_0 = 85$ mm, diameter $d_0 = 57$ mm, and density ρ_f varying in the range of 350–405 kg/m^3. Initial velocities of the projectiles, v_0, ranged from 120 m/s to 280 m/s, providing a projectile momentum per unit area $I_0 = \rho_f l_0 v_0$ of up to 9 kPa·s. To accurately evaluate the impacting response of the sandwich beam with two clamped ends, there were a total of 6 M10 bolts on the clamping device at the end of the barrel, with the 3 bolts located at each side of the clamp. High speed camera (I-SPEED 716, IX) was used to observe the dynamic deformation process of the beam, with a frame rate and exposure time of 20,000 fps and 1 μs, respectively. After test, each sandwich beam was examined to measure its permanent mid-span deflection and core compressive strain.

3. Experimental results

Table 2 summarized all the experiments performed on both empty corrugated sandwich beams (EC) and sand-filled corrugated sandwich beams (SC), including the mass of empty beam m_b, the mass of filling sand m_s, the permanent front face deflection w_f, the back face deflection w_b, and the core compressive strain ε_c. For each type of beam, 6 levels of initial momentum per unit area I_0 were applied by varying the initial velocity v_0 of the foam projectile, as detailed in Table 2.

3.1. Dynamic deformation processes

Figs. 6 and 7 displayed the time evolutions of deformation processes for empty and sand-filled sandwich beams (EC-3, 5 and SC-3, 5) under representative impulses $I_0 = 5.4$ and 7.6 kPa·s, with the response time marked on each high-speed image measured from the instant of foam impact.

Judging from the high-speed photographic sequences of empty sandwich beams (Figs. 6a and 7a), the overall structural responses of the two cases were similar. When the projectile hit the mid-span of the beam, its front face sheet began to deform and the corrugated core at the impact location began to compress with high order buckling modes. There was momentum transfer from front face to the core and back face. Subsequently, the velocity of front face decelerated while the back face accelerated and began to deform. Core compression ended when the velocities of the two face sheets became equal. Plastic hinges, initiated near the boundary of impact location, travelled towards the mid-span and supports of the beam as shown in Figs. 6a and 7a. When the plastic hinges reached the supports, stationary plastic hinges formed at the mid-span and ends of the beam at around 1.1 ms and 0.9 ms for EC-3 and EC-5, respectively. Large shear stress between the face sheets and corrugated core ensued, which might lead to failure of the braze joints, as shown in Figs. 6a and 7a. After that, the empty beams EC-3 and EC-5 attained separately their maximum deflections approximately at 1.4 ms and 1.2 ms, with certain elastic spring-back happening thereafter.

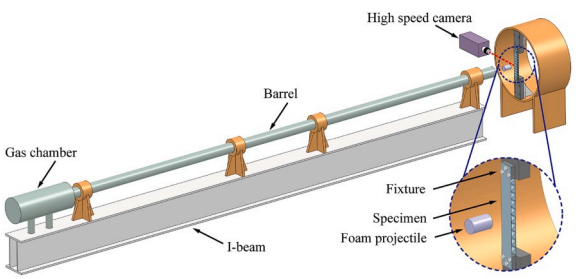

Fig. 5. Experimental set-up for foam projectile impact.

Although the two empty beams EC-3 and EC-5 exhibited similar overall structural responses, differences still existed due to different initial impulses. When the front and back face sheets achieved the same velocity, the core at the impact location of EC-3 was only partially compressed, while the core of EC-5 was compressed to full densification. Further, when travelling plastic hinges reached the supports, the motion of specimen EC-3 almost arrested. In contrast, specimen EC-5 was still in motion, and the large shear stress between the core and face sheets caused much more braze joints failure than specimen EC-3.

For comparison, Figs. 6b and 7b presented the overall deformation processes of sand-filled sandwich beams. Similar to the empty beams, the front face began to deform and the core began to buckle when the foam projectile impacted the front face of sand-filled beam. However, deflection of corrugation members (struts) was significantly reduced due to strong lateral support from the surrounding sand column. As the hybrid core had a higher strength, the core compressive strain of the two sand-filled specimens nearly did not change when the initial impulse was varied, which was quite different from the empty beams. As a result of core compression, the interstice volume in the corrugated core was reduced and the sealing tapes were impacted from the filled sand, causing the tapes to swell outwards. Similar to the empty beams, plastic hinges initiated and then travelled towards the mid-span and supports of the beam, as shown in Figs. 6b and 7b. Travelling plastic hinges arrived at the supports at around 1.4 ms for SC-3 (Fig. 6b) and 1.2 ms for SC-5 (Fig. 7b), which were later than their empty counterparts. This indicated that plastic hinges in sand-filled beams travelled more slowly than those in empty beams. When these plastic hinges reached the supports, large shear deformation ensued in the sealing tapes, causing them to wrinkle, especially near both ends of the beam; Figs. 6b and 7b. Despite significant deformation of the sealing tapes, no sand leakage occurred during the impact, suggesting that these tapes had sufficiently high adhesive strength. Sand-filled beams EC-3 and EC-5 attained their maximum deflections approximately at 1.9 ms and 1.7 ms, respectively, also later than the corresponding empty beams.

Table 2
Summary of dynamic experiments performed on empty corrugated sandwich beams (EC) and sand-filled corrugated sandwich beams (SC).

Specimen	Structure description		Foam projectile			Impacting response		
	m_b/g	m_s/g	ρ_f/kg·m^{-3}	v_0/m·s^{-1}	I_0/kPa·s	w_f/mm	w_b/mm	ε_c
EC-1	1275.6	/	361.8	119	3.6	30.6	26.7	0.22
EC-2	1261.4	/	369.3	140	4.3	36.8	30.8	0.34
EC-3	1264.2	/	372.1	173	5.4	42.0	32.9	0.51
EC-4	1256.2	/	378.6	194	6.2	45.8	36.1	0.54
EC-5	1256.6	/	365.6	245	7.6	50.5	38.4	0.68
EC-6	1272.0	/	383.2	278	9.0	55.4	43.2	0.68
SC-1	1239.6	413.8	366.5	123	3.8	21.7	20.8	0.05
SC-2	1253.6	422.0	376.7	143	4.6	24.8	23.7	0.06
SC-3	1238.8	419.2	371.2	173	5.4	29.2	28.1	0.06
SC-4	1256.4	409.6	378.6	197	6.3	33.4	31.9	0.08
SC-5	1236.0	420.4	356.3	252	7.6	36.1	34.2	0.11
SC-6	1240.2	416.0	386.0	276	9.0	39.4	37.3	0.12

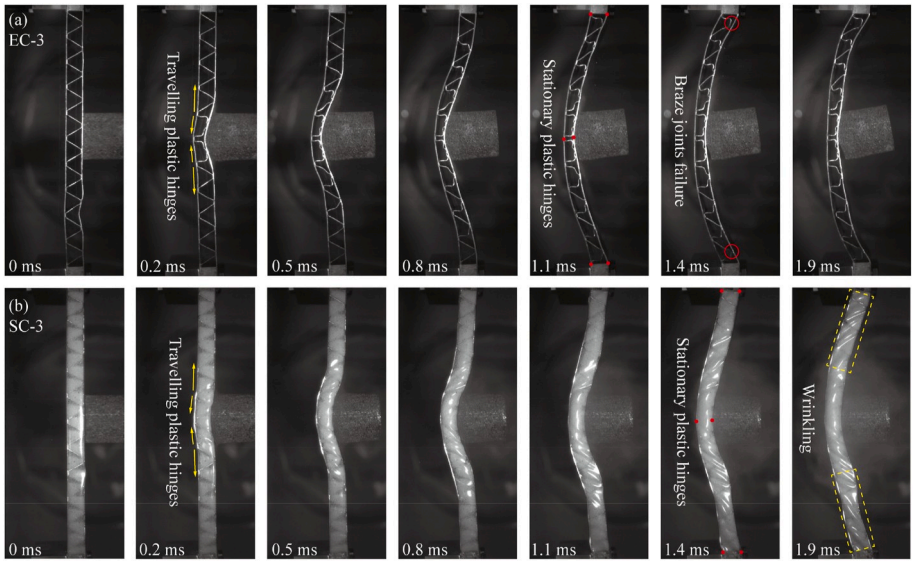

Fig. 6. High-speed photographic sequence of deformation at $I_0 = 5.4$ kPa·s: (a) empty corrugated core sandwich beam (EC-3) and (b) sand-filled corrugated core sandwich beam (SC-3).

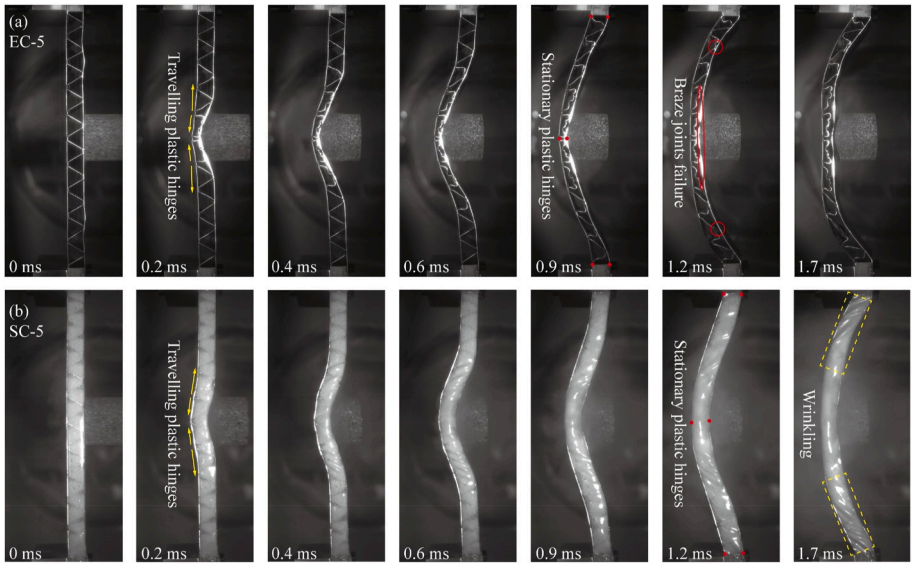

Fig. 7. High-speed photographic sequence of deformation of the (a) empty corrugated core sandwich beam (EC-5) and (b) sand-filled corrugated core sandwich beam (SC-5) for $I_0 = 7.6$ kPa·s.

3.2. Deformation and failure modes

3.2.1. Empty corrugated core sandwich beams

The measured final deflection profiles of empty sandwich beams were presented in Fig. 8a. The empty beams exhibited four different deformation/failure modes: large inelastic deformation, core compression, core shear and interfacial failure. Large inelastic deformation was the dominating deformation mode of the face sheets, caused mainly by dynamic bending and stretching. Moreover, the face sheets were so strong that no tearing or transverse shear failure was observed within the impulse range of the current study, as shown in the enlarged view of the impact area of specimen EC-6. The corrugated cores near beam mid-span deformed mainly by compression. Further, from the mid-span to the ends of the beam, the main deformation mode of the core gradually changed from core compression to core shear. As the impulse was increased, the core first underwent buckling and then progressively folded, and the amount of core crushing increased (e.g., specimens EC-1 to EC-4). For $I_0 \geq 7.6$ kPa·s (specimens EC-5 and 6), the beam could be divided into the fully folded region and the partially folded region. The fully folded region was located at the mid-span of the beam while the partially folded region was located beside it. The corrugated core in the fully folded region was fully compacted, as shown in the enlarged mid-span view of specimen EC-6 in Fig. 8a, and hence its compressive strain would not change with increasing impulse. Interfacial failure between the face sheets and core had a close correlation with the applied impulse. As the impulse was increased in magnitude, interfacial failure first occurred near the end of the beam due to large shear stressing, then happened near the impact location, as shown in the final profiles of specimens EC-3 and EC-4. Under relatively high impulse ($I_0 \geq 7.6$ kPa·s), interfacial failure was extended to the whole span of the beam as seen from the profiles of EC-5 and EC-6. Note that when the front face sheet was separated from the core, the back face sheet and the core were still connected, suggesting that brazing joints on the front face sheet were more likely to fail than those on the back face sheet.

3.2.2. Sand-filled corrugated core sandwich beams

Fig. 8b displayed the final deformed profiles of sand-filled sandwich beams, from which the deformation and failure modes could be analyzed and compared with their empty counterparts. Note that in order to clearly show the deformation of the face sheets and core, both the sealing tape on one side of the beam and the filled sand were removed after impact tests, as shown in Fig. 8b. For all the specimens, after the impact test, no tape failure or sand leakage was observed before the tape was removed, and bonding between the face sheets and the tape remained approximately intact (e.g., the enlarged view of the impact area of specimen SC-6). Similar to empty beams, large inelastic deformation was also the dominating deformation mode of the face sheets in sand-filled beams, but there existed significant difference in core deformation. Specifically, buckling and shear resistance of the sand-filled corrugated core was greatly enhanced by the filling sand as a result of its strong lateral support. The progressive folding mode observed in the empty core was absent in the sand-filled core, as only plastic buckling mode was observed by comparing the enlarged mid-span view of EC-6 with that of SC-6. Shear deformation of corrugated members in sand-filled core near the ends of the beam was significantly reduced compared with the empty ones. Further, lateral support provided by the filled sand was so strong that the amount of core crushing at impact location and core shear near the ends of the beam nearly did not change as the applied impulse was increased. Core densification also did not occur, which was quite different from the empty corrugated core. On the other hand, similar to empty beams, interfacial failure in sand-filled beams increased with increasing impulse. However, under relatively high impulse ($I_0 \geq 7.6$ kPa·s), the distribution of failure location was more random than empty beams. As the impulse was increased, the joints on both the front and back face sheets were all prone to fail (see profiles of SC-5 and 6).

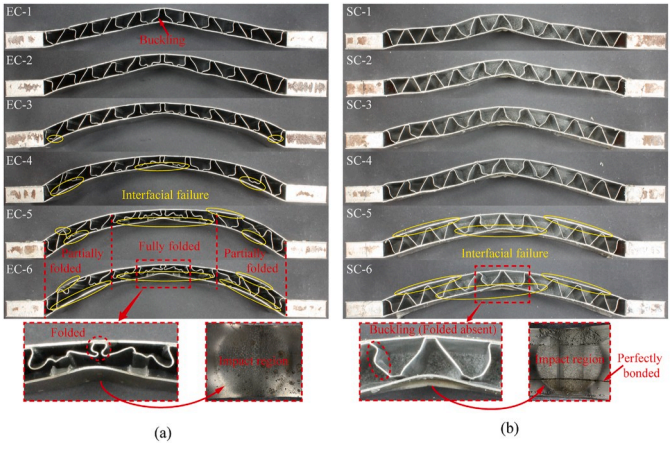

Fig. 8. Final deflection profiles of (a) empty corrugated core sandwich beams and (b) sand-filled corrugated core sandwich beams.

3.3. Beam deflection and core crushing: comparison between empty and sand-filled beams

Measurements on mid-span final deflections of front and back face sheets were presented against applied impulse in Fig. 9 for both empty and sand-filled sandwich beams. Filling sand into the core significantly reduced mid-span deflections. In the impulse regime considered, the front face deflection was reduced by about 29% in average while the back face deflection was reduced by about 16% in average. This enhancement was closely related to the higher buckling resistance of the sand-filled corrugated core. Fig. 10 compared the core compressive strains of empty beams with those of sand-filled beams. The core compressive strain of empty beams increased significantly with the increase of impulse, reaching densification strain at $I_0 = 7.6$ kPa·s. However, the core compressive strain of sand-filled beams increased much more slowly as the impulse was increased. As previously discussed, the filled sand provided strong lateral support to the corrugation members, thus significantly reducing core compressive strain. Since no significant core crushing occurred in sand-filled beams, the high second moment of area (essential to high bending resistance) was retained, leading to reduced beam deflection. In passing we note that, relative to empty beams, the enhancement effects of sand filling were not evaluated on the basis of equal mass because, sand could be easily filled into or removed from the sandwich core at low cost to deal with urgent needs and hence its added mass should not become a concern.

4. Numerical models

Three-dimensional (3D) numerical simulations were performed with commercially available software LS-DYNA v971_R8.1.0. A coupled discrete particle/finite element (FE) simulation scheme was used to simulate interaction between the filled sand, corrugation members, face sheets and sealing tapes. Sand was modeled as discrete spherical particles, while the sandwich beam, foam projectile and sealing tapes were modeled with the method of finite elements. Fig. 11 displayed the FE model for empty sandwich beams and the coupled discrete particle/FE model for sand-filled sandwich beams. Detailed description of the numerical models was provided below.

4.1. Finite element model

The deformation of empty corrugated core sandwich beams under foam projectile impact was simulated with the FE method, as shown in Fig. 11a. At the start of simulation, the metal foam projectile with a uniform velocity v_0 directly hit the mid-span of the beam. The

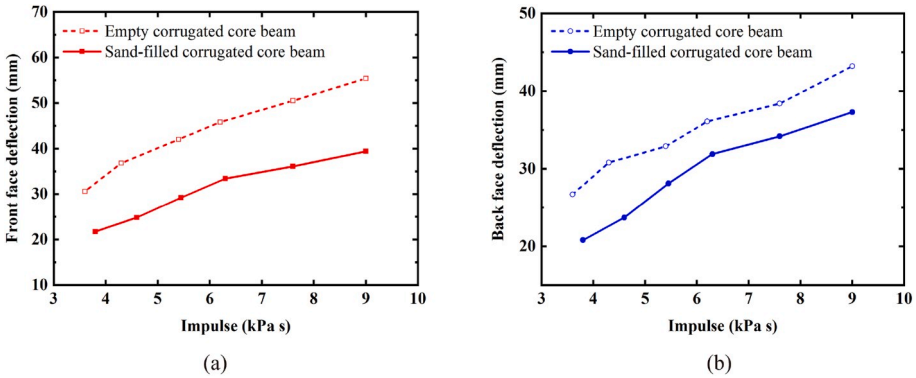

Fig. 9. Experimentally measured permanent mid-span deflections of (a) front face sheet and (b) back face sheet: comparison between empty and sand-filled corrugated core sandwich beams.

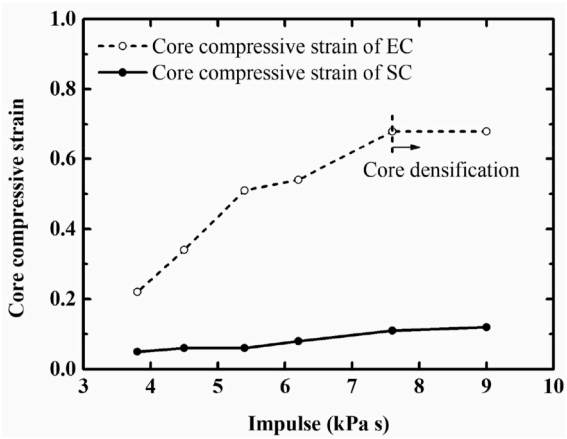

Fig. 10. Experimentally measured core compressive strain: comparison between empty and sand-filled corrugated core sandwich beams.

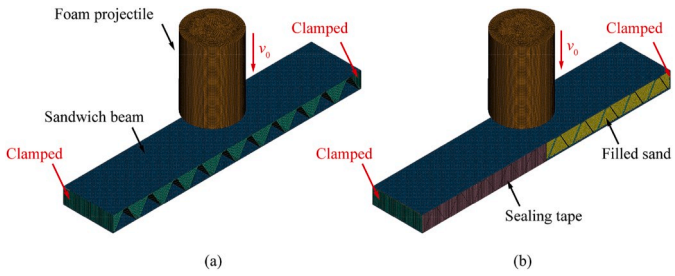

Fig. 11. (a) Finite element model for empty corrugated core sandwich beams and (b) discrete particle/finite element model for sand-filled corrugated core sandwich beams.

"CONTACT_AUTOMATIC_SURFACE_TO_SURFACE" option in LS-DYNA was employed to simulate the contact between the foam and the beam front face, with frictionless contact assumed. The foam projectile was meshed with constant stress solid elements generated by sweeping about its cylindrical axis. The sandwich beam was fully clamped at both ends, and the brazed bonding between the core and face sheets was assumed to be perfect during simulation. The face sheets and the core were both meshed using Belytschko-Tsay shell elements, with five integration points through thickness. To ensure the computational results were mesh-size insensitive, a mesh convergence study was conducted using five different mesh sizes (l_m = 0.5, 0.75, 1, 1.25, 1.5 mm). The effect of mesh size on the permanent mid-span back face deflection of empty sandwich beam EC-3 was shown in Fig. 12, with initial impact impulse I_0 = 5.4 kPa·s. The results converged when the mesh size $l_m \leq 1$ mm. Thus, an average element size of 1 mm was selected for subsequent simulations.

4.2. Coupled discrete particle/finite element model

Deformation of sand-filled corrugated core beams resulting from foam projectile impact was modeled using a coupled discrete particle/FE simulation scheme (Fig. 11b). The discrete particles of sand and their coupling with other FE structures of the model were described next.

4.2.1. Discrete particle model

The sand material was modeled using a group of 3D rigid spherical particles, each of diameter d. Since the sand used in the current experiments was dry, the effect of sand saturation was neglected. Fig. 13 displayed schematically the rheological model in LS-DYNA, characterizing the interaction between two dry particles with equal mass m.

The model of Fig. 13 consisted of a normal and a tangential spring with stiffness K_n and K_t, a normal and a tangential dashpot with damping coefficients C_n and C_t, and lastly a frictional element with a static friction coefficient μ_s and a rolling friction coefficient μ_r. Let δ_n and δ_t denote the relative normal and tangential displacements of the contacting particles. Contact forces along the normal and tangential directions could thence be described by:

$$F_n = K_n\delta_n + C_n\dot{\delta}_n \quad (2)$$

and

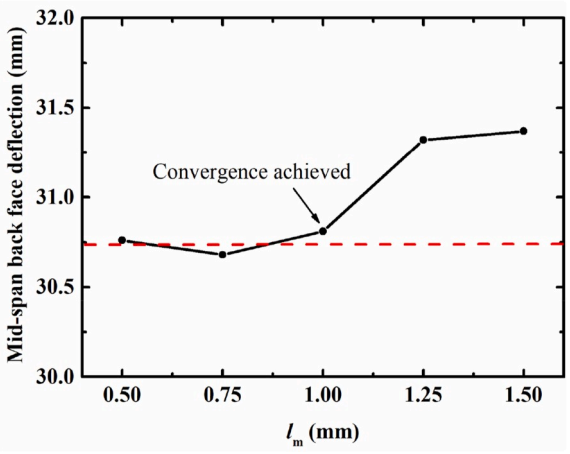

Fig. 12. Effect of mesh size on numerically predicted mid-span back face deflection of empty sandwich specimen EC-3.

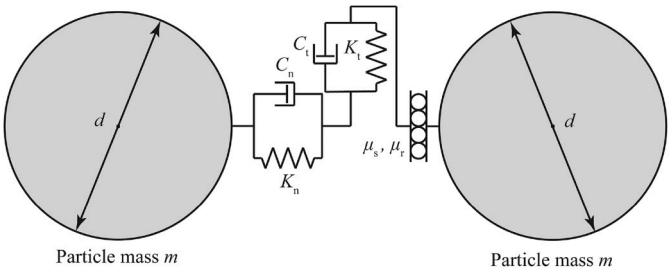

Fig. 13. Rheological model for the interaction between two identical rigid spherical particles.

$$F_t = \begin{cases} -K_t\delta_t - C_t\dot{\delta}_t & \text{if } |F_t| < |\mu_s F_n| \\ -\mu_s|F_n|sign(\delta_t) & \text{otherwise} \end{cases} \tag{3}$$

Rolling resistance of a particle was introduced via a moment M_r that tended to retard the rolling motion, given by:

$$M_r = \frac{1}{2}d{\cdot}\mu_r F_n \tag{4}$$

The normal spring stiffness K_n and tangential spring stiffness K_t in Eqs. (2) and (3) were given by:

$$K_n = \frac{k_1 d_1 k_2 d_2}{2k_1 d_1 + 2k_2 d_2} NormK = \frac{1}{4}kd{\cdot}NormK \tag{5}$$

and

$$K_t = K_n{\cdot}ShearK \tag{6}$$

where k_i and d_i were the bulk modulus and diameter of the ith particle, respectively, and *NormK* and *ShearK* were user-specified stiffness penalty parameters. In the current simulation, the particles were assumed identical, sharing the same bulk modulus k and diameter d. The bulk modulus k was directly related to the Young's modulus E and Poisson ratio ν of the particles according to $k = E/3(1-2\nu)$.

The normal damping coefficient C_n was determined by the ratio of critical damping in the normal direction, as:

$$C_n = 2.0{\cdot}NDAMP{\cdot}\sqrt{\frac{m_1 m_2}{m_1 + m_2}K_n} = NDAMP{\cdot}\sqrt{2mK_n} \quad \text{with} \quad 0 \le NDAMP \le 1 \tag{7}$$

where *NDAMP* was the normal damping parameter deciding the ratio of normal critical damping. The tangential damping coefficient C_t was defined in a similar way as Eq. (7) with *TDAMP* and K_t being used instead of *NDAMP* and K_n, respectively:

$$C_t = TDAMP{\cdot}\sqrt{2mK_t} \quad \text{with} \quad 0 \le TDAMP \le 1 \tag{8}$$

Rigid spherical particles for the filled sand were generated with the sphere packing engine in LS-PREPOST [37]. Each particle had a diameter of 0.90 mm, determined by the average size of sand grains shown in Fig. 4b. The density of sand particles was set as 2650 kg/m^3 and the initial volume fill fraction was 50%, resulting in an initial sand density of 1325 kg/m^3 that was close to that used in the experiment. Actual size distribution and angular shape of the sand particles were neglected in the simulation.

4.2.2. Coupling of discrete particle and finite element

The FE parts of the sand-filled numerical model were foam projectile, empty sandwich beam and sealing tape. Construction of the former two parts followed the previously mentioned FE model for empty sandwich beams. In view of the experimentally observed dynamic deformation processes of sand-filled beams shown in Figs. 6b and 7b, the sealing tape was assumed to be perfectly bonded to the sandwich beam. The edge of the tape, the edge of face sheets, and the ends of sandwich beam were tied together in the FE model. To this end, the sealing tape model shared the same element type and mesh size of the empty sandwich beam model.

Coupling of the discrete particles and finite elements was realized using the newly implemented routine "DEFINE_DE_TO_SURFACE_COUPLING" in LS-DYNA. This contact definition, particularly designed for discrete particles, and described the friction and damping forces in particle-structure interaction. Following Uesugi et al. [38] and Karajan et al. [39], the friction and damping coefficients for contact between the particles and sandwich beam were both set as 0.6 in the current simulation.

4.3. Material properties

4.3.1. Material constitutive models

The metal foam projectile was modeled using the foam material model, *MAT_CRUSHABLE_FOAM, for crushable foams in impact or other applications. The model described dynamic compressive behavior of the foam through the input of a stress versus volumetric strain curve. Quasi-static compressive stress versus strain behavior of the present close-celled aluminum foam was presented in Fig. 3a. Strain rate effect of the foam was considered by introducing a damping coefficient of magnitude 0.1 [40].

Material make of the sandwich beam, 304 stainless steel, was modeled using a bi-linear elasto-plastic constitutive model, *MAT_PLASTIC_KINEMATIC, with the option of including strain rate effect. The measured uniaxial tensile true stress versus strain curve of Fig. 3b was employed using the prescription described in Section 2.2. Strain rate sensitivity was accounted for by using the Cowper-Symonds relation given by Eq. (9):

$$\frac{\sigma_d}{\sigma_y} = 1 + \left(\frac{\dot{\varepsilon}}{C}\right)^{\frac{1}{P}} \tag{9}$$

where σ_d and σ_y were the dynamic and static yield strength, $\dot{\varepsilon}$ was the strain rate, and C and P were the user defined input constants. A previous study found that the effect of brazing step during the fabrication of 304 stainless steel was similar to annealing treatment [41]. Consequently, $C = 3398.47$ s^{-1} and $P = 6.17$ were obtained by fitting existing experimental results of annealed 304 stainless steel at different strain rates [41,42], as shown in Fig. 14.

Material make of the sealing tape was modeled using a two-parametric rubber model, *MAT_MOONEY-RIVLIN_RUBBER. According to the Mooney-Rivlin theory [43,44], the strain energy density W for an incompressible material was defined as:

$$W = A(I_1 - 3) + B(I_2 - 3) \tag{10}$$

where A and B were two constant coefficients, and I_1 and I_2 were the first and second invariants of the Cauchy-Green tensor:

$$I_1 = \lambda_1^2 + \lambda_2^2 + \lambda_3^2 \tag{11}$$

$$I_2 = \lambda_1^2\lambda_2^2 + \lambda_1^2\lambda_3^2 + \lambda_2^2\lambda_3^2 \tag{12}$$

Here, λ_1, λ_2 and λ_3 were the stretch ratios in three principal directions. In the case of uniaxial tension, the three stretch ratios could be simplified as: $\lambda_1 = \lambda$, $\lambda_2 = \lambda_3 = 1/\lambda^{0.5}$. Relation between uniaxial tensile stress σ and uniaxial stretch ratio λ could thence be obtained by taking the derivative of strain energy density with respect to stretch ratio, as:

$$\sigma = \frac{dW}{d\lambda} = \left(2A + \frac{2B}{\lambda}\right)\left(\lambda - \frac{1}{\lambda^2}\right) \tag{13}$$

where $\lambda = 1 + \varepsilon$. Upon fitting the uniaxial tensile curve of Fig. 3c, the two coefficients in the material model were obtained as $A = 0.51$ MPa and $B = 2.56$ MPa. The fitted curve using the foregoing coefficients

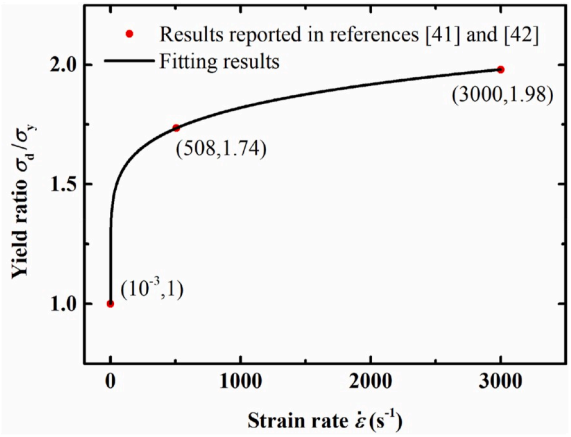

Fig. 14. Strain rate effects of annealed 304 stainless steel: experimental data and fitting results with Cowper-Symonds model.

agreed well with the experimental results, as shown in Fig. 15.

Sand was modeled with rigid discrete particles, with its mechanical properties determined by contact forces between the particles. In LS-DYNA, the card *MAT_ELASTIC was used to determine the mechanical properties of particles needed in the contact model. In this card, the mass density ρ determined the density of sand particles, while the Young's modulus E and Poisson ratio ν determined the bulk modulus k in Eq. (5) via $k = E/3(1-2\nu)$. Note that although the "ELASTIC" material card was used, the sand particles in the simulation were still treated as rigid. Typical values selected for the low-quartz were [45]: $\rho = 2650$ kg/m^3, $E = 95.6$ GPa and $\nu = 0.084$. For completeness, Table 3 listed all the material constants used in the current numerical simulations.

4.3.2. Calibration of contact properties of discrete particles

An important factor in discrete particle modeling was the correct determination of input parameters for LS-DYNA concerning the contact properties between particles. In the current study, slump test and constrained compression test were used to calibrate the contact parameters. The former was used to estimate the friction between particles while the latter was used to estimate the contact stiffness. Note that damping forces between the particles were not included in this section due to the lack of test data, but the effect of damping was considered in the next section. Therefore, four parameters in the contact model, μ_s, μ_r, K_n and K_t, were calibrated, as detailed below.

In the slump test, a cylindrical tube filled with sand, diameter 31.5 mm and height 18.5 mm, was placed on a rigid 304 stainless steel plate (shown in Fig. 16a). Both the sand and stainless steel were the same as those used in the experiment. The tube was then lifted slowly to form a sand pile, as shown in Fig. 16b. Subsequently, numerical simulations of slump test with varying values of μ_s and μ_r were conducted: the numerically simulated shape of sand pile agreed well with experiment when $\mu_s = 0.5$ and $\mu_r = 0.2$ (Fig. 16c).

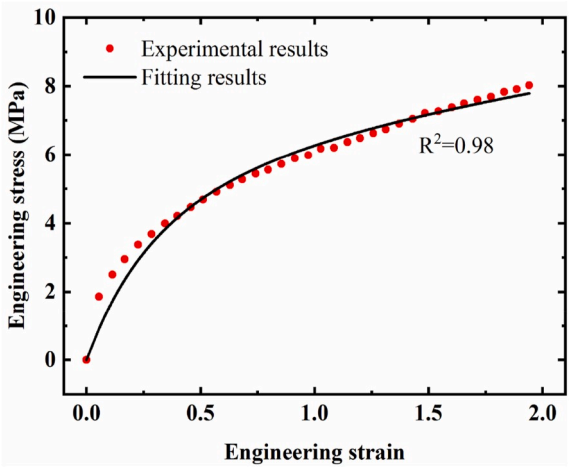

Fig. 15. Nominal stress versus strain curve of sealing tape: experimental measurement and fitting result with Mooney-Rivlin model.

The measured constrained compressive response of sand (Fig. 3d) was used to estimate the inter-particle stiffness K_n and K_t used in the model. Spherical sand particles were packed into a rigid container as sketched in the inset of Fig. 17. These spherical particles had a diameter of 0.9 mm and an initial volume fraction of 0.5, same as those in the experiment. Based on slump test results, the friction coefficients μ_s and μ_r were set as 0.5 and 0.2, respectively, and the suggested ratio $K_t/K_n = 2/7$ ($ShearK = 2/7$) was used in accordance with Karajan et al. [39]. Numerical simulations of the compression test were conducted by compressing the discrete particles via a rigid punch, as shown in the inset of Fig. 17. The predicted nominal strain versus nominal stress responses were presented in Fig. 17 for three choices of contact stiffness K_n, with the remaining contact parameters kept constant. The results of Fig. 17 indicated that when $K_n = 0.3$ MN/m ($NormK = 0.035$), the predictions agreed well with experimental measurements.

5. Numerical results and discussion

5.1. Model validation

As energy conservation of the whole system is the premise of obtaining correct numerical results, it was firstly investigated. Fig. 18 presented the predicted energy-time curves of empty specimen EC-3 and sand-filled specimen SC-3. It is seen that the total energy was equal to the sum of kinetic energy, internal energy, sliding energy and hourglass energy. Good energy balance was achieved since the sliding energy and hourglass energy were small, much less than 10% of the internal energy. For both the empty and sand-filled sandwich beams, the initial kinetic energy of foam projectile was mostly converted into the internal energy of the whole system.

Fig. 19a displayed the numerically calculated pressure versus time histories exerted by foam projectile on the front faces of empty specimen EC-3 and sand-filled specimen SC-3. When struck by foam projectile, pressure on the front face first increased sharply from zero to a peak and then rapidly decreased to zero. While the two curves of empty and sand-filled beams exhibited similar overall variation trends, the relatively small discrepancies were attributed to the differences in their intrinsic impact resistances. The impact impulse per unit area transferred by foam projectile to each specimen was calculated by integrating the pressure versus time history in Fig. 19a. The results shown in Fig. 19b suggested that the impulses transmitted to both beams increased quickly and then reached the same stable value of 5.7 kPa·s, close to the initial momentum of foam projectile $I_0 = 5.4$ kPa·s in the experiment.

Fig. 20 presented the numerically predicted mid-span deflection versus time histories of specimens EC-3 and SC-3, with $I_0 = 5.4$ kPa·s selected for both types of sandwich beam. Irrespective of the sandwich type, the curve increased monotonously to the maximum deflection, followed by small oscillations around a plateau value due to elastic spring back. Note that the empty sandwich beam achieved its maximum deflection faster than the sand-filled one, same as that observed in the current experiments. Further, the oscillation amplitude of EC-3 was larger than that of SC-3, suggesting that sand filling reduced vibration in the elastic spring back stage.

For both empty and sand-filled sandwich beams, the numerically predicted final deformation profiles were compared with those experimentally observed in Fig. 21. The simulations predicted large inelastic bending of the beams due to plastic deformation and core compression due to buckling, and the predicted final deformation profiles agreed well with those measured in the experiments. The predicted permanent mid-

Table 3
Material card specifications for numerical simulations.

*MAT_CRUSHABLE_FOAM (foam projectile — material type 63 in LS-DYNA)								
MID	RO/kg·m^{-3}	E/Pa	PR	LCID	TSC	DAMP		
1	378	1E+9	0	Fig. 3a	7.1E-3	0.1		
*MAT_PLASTIC_KINEMATIC (sandwich beam — material type 3 in LS-DYNA)								
MID	RO/kg·m^{-3}	E/Pa	PR	SIGY/Pa	ETAN/Pa	BETA	SRC/s^{-1}	SRP
2	7800	2E+11	0.3	1.8E+8	2E+9	0	3398.47	6.17
* MAT_MOONEY-RIVLIN_RUBBER (sealing tape — material type 27 in LS-DYNA)								
MID	RO/kg·m^{-3}	PR	A/Pa	B/Pa				
3	1143	0.495	5.1E+5	2.56E+6				
*MAT_ELASTIC (sand —material type 1 in LS-DYNA)								
MID	RO/kg·m^{-3}	E/Pa	PR					
4	2650	9.56E+10	0.084					

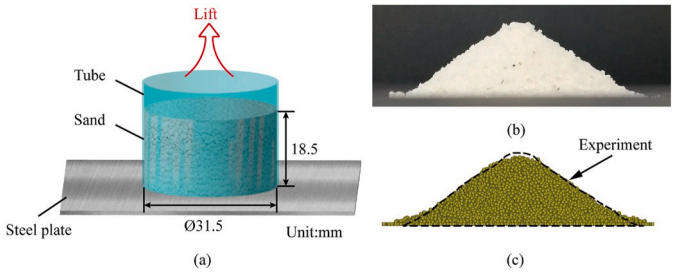

Fig. 16. (a) Sketch of slump test setup, (b) photograph of sand pile after slump test, and (c) numerically simulated sand profile of slump test.

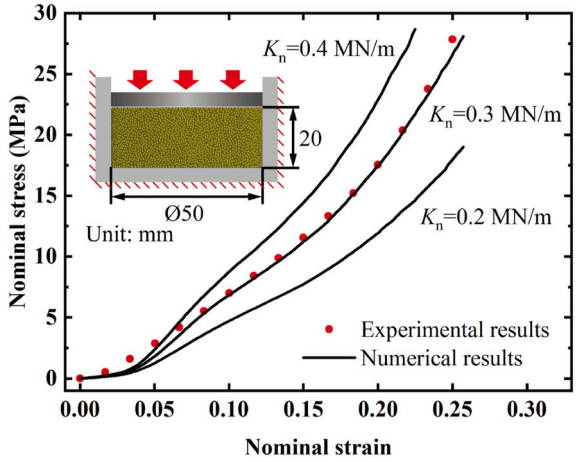

Fig. 17. Comparison between experimental measurements and numerical predictions of constrained compression response of sand.

span deflections of empty and sand-filled sandwich beams were compared in Fig. 22 with experimental measurements. The permanent deflection was calculated by averaging the displacement over several cycles of elastic vibration (from trough to peak) in the deflection versus time curve. The results of Fig. 22 showed that, relative to experimental data, the numerically calculated the permanent mid-span deflection exhibited similar variation trend as the impulse was increased. However, for both types of sandwich beams, there was some difference between the numerical and experimental results, although the difference was no more than 30%. The difference may be attributed to four possible reasons, summarized as follows.

(I) The face sheets and the sandwich core were tied together in FE simulations, and brazing joints failure observed in experiments were not considered in the simulation. As a result, the predicted and measured buckling modes of the core webs having failed joints were different in Fig. 21. Under high impulses, more brazing joints would fail, which likely caused the relatively large discrepancy of deflections for the empty beams in Fig. 22.

(II) The clamped boundary condition assumed in the simulation was not fully representative of actual experimental situation. In the experiment, the boundary of the beam may move under impact, especially for high velocity impact. Accordingly, the predicted and measured bending modes of EC-5 and EC-6 were different near the boundary, which may also contribute to the discrepancy of deflections for empty beams under high impulses in Fig. 22.

(III) Manufacturing defects in sandwich beams were not considered in FE simulations, which might affect the numerical results. Under low velocity impact, unusual bending of face sheets was observed from the measured profiles of SC-1, 2 and 3 in Fig. 21, which was probably caused by manufacturing defects. Such face sheet bending was not captured by FE simulations. In addition, as manufacturing defects led to greater mid-span deformations of the beams under relatively low pulses, the underestimation of FE simulations was expected in Fig. 22.

(IV) Different from real sand particles in the experiments, sand particles were idealized as spherical particles of identical size in FE simulations which might also contribute to the difference, especially under low velocity impact. Therefore, the discrepancies between numerical and experimental results were relatively large for sand-filled beams under low impulse in Fig. 22.

5.2. Discussion

The nature of sand and many other sand-like materials varies widely, and this difference would influence sand-structure interaction closely related to the shock resistance of sand-filled, hybrid-cored sandwich beams. Given that the present numerical predictions agreed well with experimental measurements, the numerical models were further utilized to investigate the effects of sand properties. Again, resistance to foam projectile impact was quantified in terms of permanent mid-span deflection, with the impulse fixed at $I_0 = 5.4$ kPa·s.

5.2.1. Density of sand

The density of dry sand was dictated by two factors: (I) composition of sand grains, namely density of sand grains, and (II) initial porosity of sand. Here, the effect of density of sand was explored by varying the density of sand particles while maintaining the initial volume fill fraction of sand at 50%. Fig. 23a illustrated how sand density affected the mid-span beam deflections. Deflections of both the front and back face

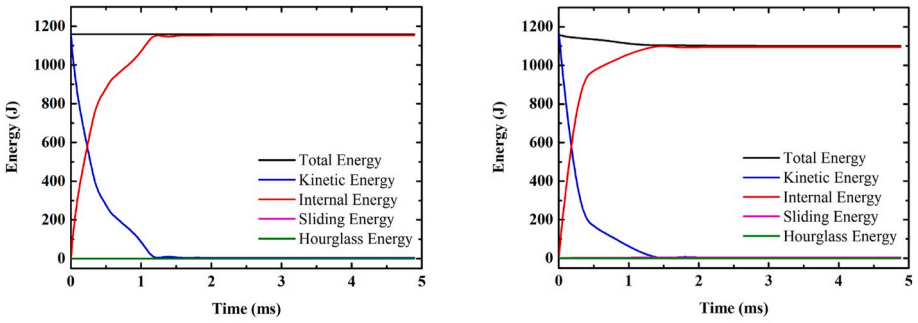

Fig. 18. Numerically predicted energy-time curves of (a) empty sandwich beam EC-3 and (b) sand-filled sandwich beam SC-3.

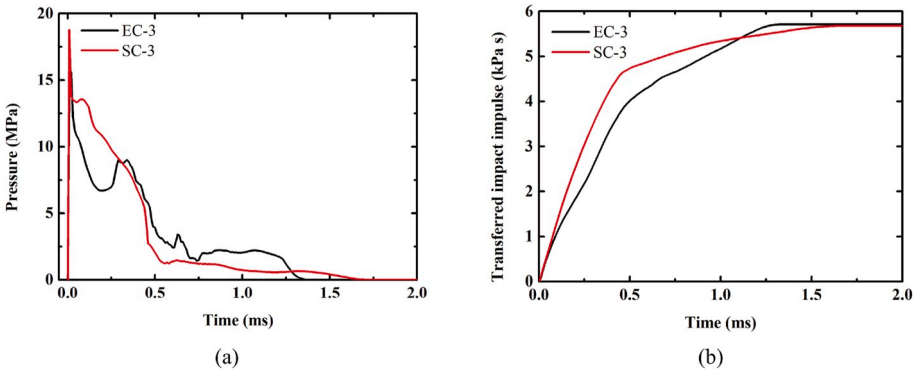

Fig. 19. Numerically predicted (a) pressure versus time histories and (b) corresponding transferred impulse versus time histories exerted by foam projectiles on empty sandwich beam EC-3 and sand-filled sandwich beam SC-3.

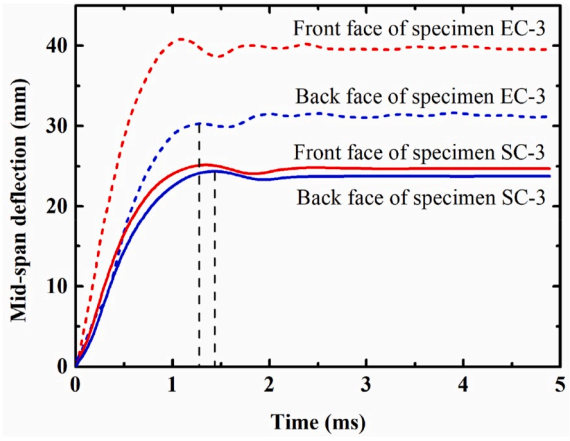

Fig. 20. Numerical predictions of mid-span deflections versus time histories of specimens EC-3 (empty core) and SC-3 (sand-filled core).

sheets increased significantly with decreasing density of the filled sand. In the limit when the sand density approached zero, the back face deflection was close to that of the empty beam, while the front face deflection was still much smaller than the empty case. This indicated that the additional mass provided by the filled sand could increase the inertial resistance, thus providing additional shock protection. This additional inertial resistance played an important role in reducing face sheet deformation, especially the back face sheet.

5.2.2. Stiffness of sand

The stiffness of sand was controlled by penalty based particle-particle contact stiffness in the discrete particle model. The normal contact stiffness K_n was determined by bulk modulus k and grain size d according to Eq. (5). In this section, by fixing the grain size at 0.9 mm, the effect of K_n was evaluated by varying the bulk modulus of sand particles. Simultaneously, the tangential contact stiffness K_t was determined by Eq. (6), where $ShearK = 2/7$ as suggested by Karajan et al. [39]. Fig. 23b plotted the mid-span deflection as a function of the normal contact stiffness. The results revealed that when the contact stiffness decreased, the strength of sand-filled core decreased, resulting in more energy dissipation via deformation of the front face and core and, correspondingly, less energy dissipation by the back face. Also, the reduced core strength led to smaller residual bending strength of the entire sandwich structure after core compression, thus increasing the deflections of both the front and back faces. As a result of the combined effects of the two mechanisms, the front face deflection increased with decreasing contact stiffness, while the back face deflection first decreased and then increased. When the normal contact stiffness had a value of about 1 kN/m, the back face deflection reached its minimum as shown in Fig. 23b.

5.2.3. Inter-particle friction

Friction between sand particles could be classified into sliding friction and rolling friction. Sliding friction between sand particles was mainly determined by surface roughness, but rolling friction was also influenced by the actual shape and size distribution of sand grains. Here, for simplicity, the effects of actual particle shape and size distribution on inter-particle friction were neglected, and only sliding friction between particles was discussed. With sliding friction in the discrete particle model was described by Eq. (3), its influence on mid-span deflection was evaluated by altering the sliding friction coefficient μ_s as shown in Fig. 23c for selected values of μ_s. When μ_s was relatively low, the front face deflection decreased with increasing friction while that of the back face increased. However, when the sliding friction coefficient became

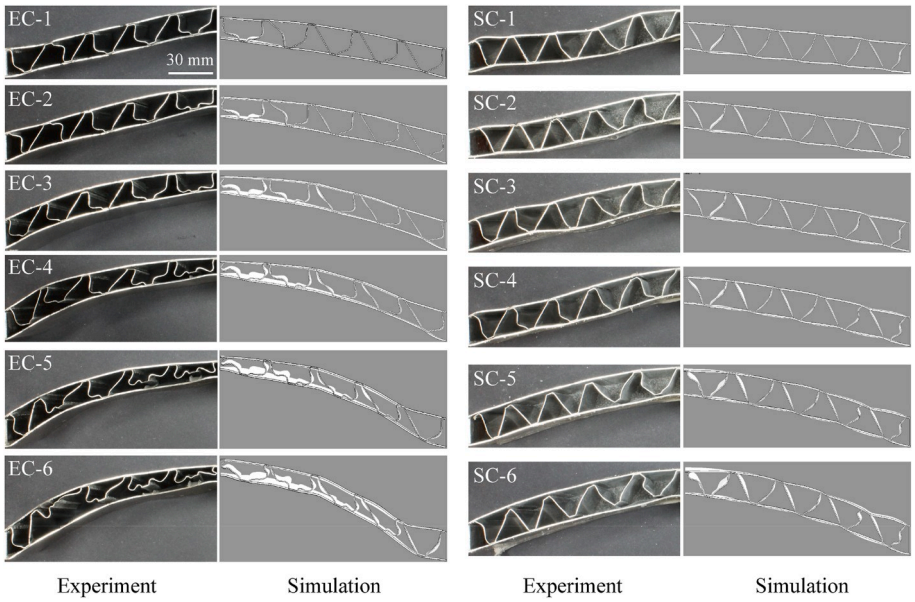

Fig. 21. Comparison between the measured and predicted final deformation profiles of empty and sand-filled sandwich beams.

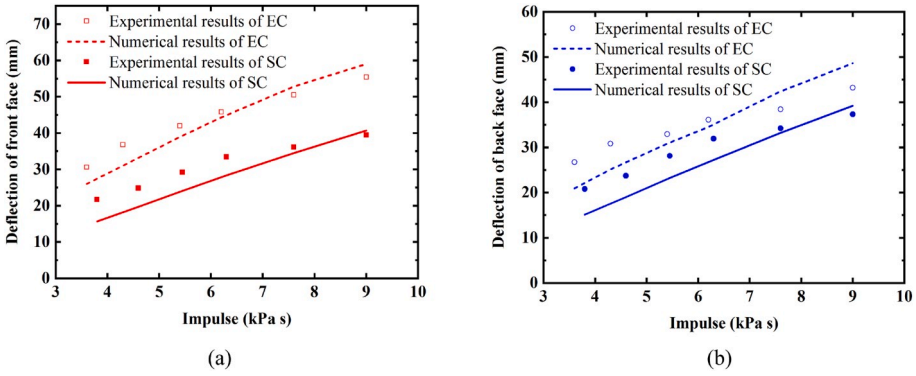

Fig. 22. Permanent mid-span deflections of (a) front face sheet and (b) back face sheet plotted as functions of impulse for both empty corrugated beams (EC) and sand-filled corrugated beams (SC): comparison between experimental and numerical results.

sufficiently large, it had no effect on beam deflection. That is, in the presence of high inter-particle friction, it was more difficult for the filled sand to flow under impact. Correspondingly, the sand-filled core became stronger, resulting in smaller front face deflection and larger back face deflection. When the friction coefficient was increased to a critical value, sliding friction between sand particles was sufficiently strong so that further increasing the friction had little effect on the flow characteristics of sand as well as beam deflection.

5.2.4. *Inter-particle damping*

The effect of damping between sand particles was evaluated by varying the ratio of critical damping *NDAMP* and *TDAMP* in Eqs. (7) and (8). For simplicity, damping coefficients in the normal and tangential directions were assumed equal: $NDAMP = TDAMP = \xi$. The ratio of critical damping ξ determined the coefficient of restitution during collisions of sand particles. When $\xi = 0$, collision between sand particles was elastic and, when $\xi = 1$, the collision was fully plastic. Fig. 23d plotted beam deflection as a function of critical damping ratio, which showed that damping forces during collisions of sand particles had no effect on the shock resistance of sand-filled beams. In other words, the energy dissipated by the collisions was negligibly small during shock loading.

6. Concluding remarks

Dynamic responses of fully clamped, sand-filled corrugated core sandwich beams under simulated shock loading with aluminum foam projectile were experimentally characterized. A numerical model was established using coupled discrete particle/finite element method and validated against experimental measurements. The validated numerical model was then utilized to evaluate how the key properties of filled sand affect beam shock resistance. Main findings were summarized as follows.

(1) Sand filling significantly enhanced the shock resistance of corrugated core sandwich beams, for sand filling not only increased the inertial resistance (thus additional shock protection) but also provided strong lateral support to corrugated members against deformation and buckling.
(2) The coupled discrete particle/finite element approach predicted reasonably well the primary features of sand-filled sandwich beams observed experimentally.
(3) Different sand properties affected the shock resistance of sand-filled beams in different manners. The density and stiffness of sand significantly affected the beam shock resistance, followed by

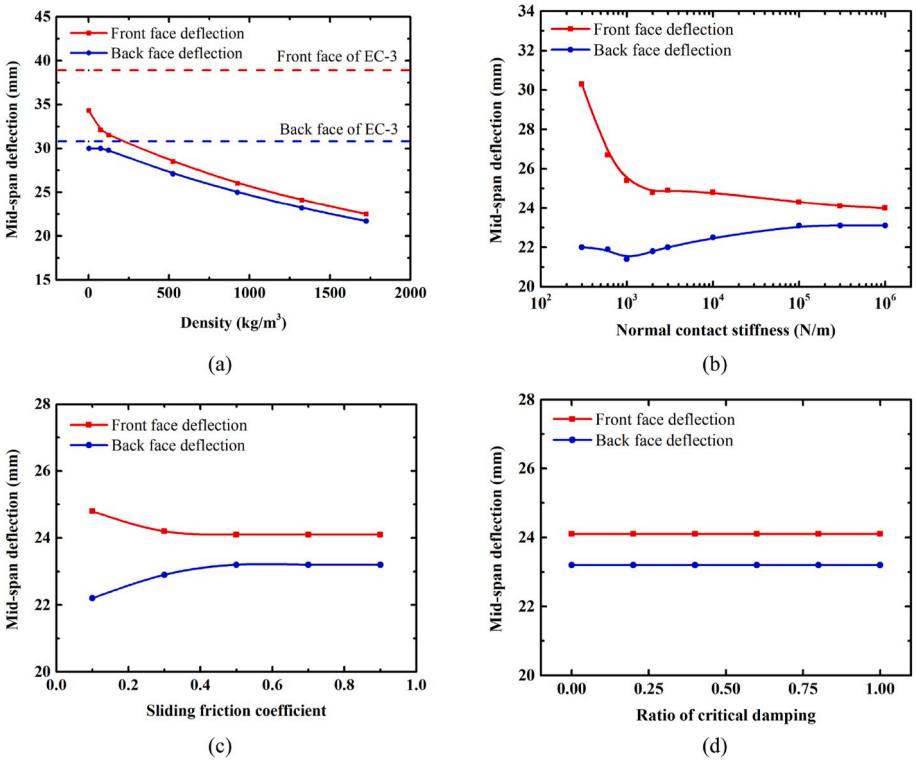

Fig. 23. Effect of (a) density, (b) stiffness, (c) inter-particle sliding friction and (d) inter-particle damping of filled sand on front and back face mid-span deflections.

inter-particle friction, whereas inter-particle damping played a negligible role.

(4) Increasing the sand density significant led to significantly reduced permanent beam deflection. As the sand stiffness was increased, the front face deflection increased while the back face deflection first decreased and then increased. Increasing the sliding friction between sand particles reduced the deflection of front face, but increased the deflection of back face.

The experimental and numerical results of this study are helpful for designing maneuverable, quickly installed temporary protective structures to shield schools, hospitals, embassies and other vital facilities in urgent situations.

Declaration of competing interest

The authors declare that they have no known competing financial interests or personal relationships that could have appeared to influence the work reported in this paper.

CRediT authorship contribution statement

Run-Pei Yu: Conceptualization, Methodology, Software, Writing - original draft, Writing - review & editing. **Xin Wang:** Investigation, Data curation. **Qian-Cheng Zhang:** Formal analysis, Writing - review & editing. **Lang Li:** Software, Visualization. **Si-Yuan He:** Resources, Investigation. **Bin Han:** Investigation. **Chang-Ye Ni:** Resources. **Zhen-Yu Zhao:** Validation. **Tian Jian Lu:** Funding acquisition, Conceptualization, Supervision.

Acknowledgments

This work was supported by the National Key Research and Development Program of China (2017YFB1102801), the Open Project for Key Laboratory of Intense Dynamic Loading and Effect (KLIDLE1801), the National Natural Science Foundation of China (11972185), the Aviation Science Foundation Project (20170970002), the Open Fund of the State Key Laboratory of Mechanics and Control of Mechanical Structures (Nanjing University of Aeronautics and astronautics, MCMS-E0219K02) and the Open Project of State Key Laboratory of Smart Manufacturing for Special Vehicles and Transmission System (GZ2019KF015).

References

[1] Hoemann JM, Salim H. Experimental evaluation of structural composites for blast resistant design, vol. 1466516. University of Missouri-Columbia; 2007. p. 91.
[2] Børvik T, Hanssen AG, Dey S, Langberg H, Langseth M. On the ballistic and blast load response of a 20 ft ISO container protected with aluminium panels filled with a local mass - phase I: design of protective system. Eng Struct 2008;30:1605–20.
[3] Børvik T, Burbach A, Langberg H, Langseth M. On the ballistic and blast load response of a 20ft ISO container protected with aluminium panels filled with a local mass - phase II: validation of protective system. Eng Struct 2008;30:1621–31.
[4] Ahmed S, Galal K. Effectiveness of FRP sandwich panels for blast resistance. Compos Struct 2017;163:454–64.
[5] Hussein A, Mahmoud H, Heyliger P. Probabilistic analysis of a simple composite blast protection wall system. Eng Struct 2020;203:109836.
[6] Jing L, Wang Z, Ning J, Zhao L. The dynamic response of sandwich beams with open-cell metal foam cores. Compos B Eng 2011;42:1–10.
[7] Ye N, Zhang W, Li D, Huang W, Xie W, Huang X, et al. Dynamic response and failure of sandwich plates with PVC foam core subjected to impulsive loading. Int J Impact Eng 2017;109:121–30.
[8] Chen D, Jing L, Yang F. Optimal design of sandwich panels with layered-gradient aluminum foam cores under air-blast loading. Compos B Eng 2019;166:169–86.
[9] Sun G, Wang E, Zhang J, Li S, Zhang Y, Li Q. Experimental study on the dynamic responses of foam sandwich panels with different facesheets and core gradients subjected to blast impulse. Int J Impact Eng 2020;135:103327.
[10] Dharmasena KP, Wadley HNG, Xue Z, Hutchinson JW. Mechanical response of metallic honeycomb sandwich panel structures to high-intensity dynamic loading. Int J Impact Eng 2008;35:1063–74.
[11] Liu J, Wang Z, Hui D. Blast resistance and parametric study of sandwich structure consisting of honeycomb core filled with circular metallic tubes. Compos B Eng 2018;145:261–9.
[12] Zhang Y, Liu Q, He Z, Zong Z, Fang J. Dynamic impact response of aluminum honeycombs filled with Expanded Polypropylene foam. Compos B Eng 2019;156:17–27.
[13] Li Y, Chen Z, Xiao D, Wu W, Fang D. The Dynamic response of shallow sandwich arch with auxetic metallic honeycomb core under localized impulsive loading. Int J Impact Eng 2020;137:103442.

[14] Rubino V, Deshpande VS, Fleck NA. The dynamic response of end-clamped sandwich beams with a Y-frame or corrugated core. Int J Impact Eng 2008;35:829–44.
[15] Li X, Wang Z, Zhu F, Wu G, Zhao L. Response of aluminium corrugated sandwich panels under air blast loadings: experiment and numerical simulation. Int J Impact Eng 2014;65:79–88.
[16] Zhang P, Cheng Y, Liu J, Wang C, Hou H, Li Y. Experimental and numerical investigations on laser-welded corrugated-core sandwich panels subjected to air blast loading. Mar Struct 2015;40:225–46.
[17] Rong Y, Liu J, Luo W, He W. Effects of geometric configurations of corrugated cores on the local impact and planar compression of sandwich panels. Compos B Eng 2018;152:324–35.
[18] Wang X, Yu RP, Zhang QC, Li L, Li X, Zhao ZY, et al. Dynamic response of clamped sandwich beams with fluid-fillied corrugated cores. Int J Impact Eng 2020;139:103533.
[19] Dharmasena KP, Wadley HNG, Williams K, Xue Z, Hutchinson JW. Response of metallic pyramidal lattice core sandwich panels to high intensity impulsive loading in air. Int J Impact Eng 2011;38:275–89.
[20] Jin N, Wang F, Wang Y, Zhang B, Cheng H, Zhang H. Effect of structural parameters on mechanical properties of Pyramidal Kagome lattice material under impact loading. Int J Impact Eng 2019;132.
[21] Li Z, Chen W, Hao H. Functionally graded truncated square pyramid folded structures with foam filler under dynamic crushing. Compos B Eng 2019;177:107410.
[22] Xue Z, Hutchinson JW. A comparative study of impulse-resistant metal sandwich plates. Int J Impact Eng 2004;30:1283–305.
[23] Rimoli JJ, Talamini B, Wetzel JJ, Dharmasena KP, Radovitzky R, Wadley HNG. Wet-sand impulse loading of metallic plates and corrugated core sandwich panels. Int J Impact Eng 2011;38:837–48.
[24] Yazici M, Wright J, Bertin D, Shukla A. Preferentially filled foam core corrugated steel sandwich structures for improved blast performance. J Appl Mech Trans ASME 2015;82:1–13.
[25] Zhang P, Cheng Y, Liu J, Li Y, Zhang C, Hou H, et al. Experimental study on the dynamic response of foam-filled corrugated core sandwich panels subjected to air blast loading. Compos B Eng 2016;105:67–81.
[26] Wadley HNG, Dharmasena KP, O'Masta MR, Wetzel JJ. Impact response of aluminum corrugated core sandwich panels. Int J Impact Eng 2013;62:114–28.
[27] Wu X, Xiao K, Yin Q, Zhong F, Huang C. Experimental study on dynamic compressive behaviour of sandwich panel with shear thickening fluid filled pyramidal lattice truss core. Int J Mech Sci 2018;138–139:467–75.
[28] Edwards MR, Palmer ME. Mitigation of comminution effects of explosives by particulate materials. J Appl Phys 2003;93:2540–3.
[29] Britan A, Shapiro H, Ben-Dor G. The contribution of shock tubes to simplified analysis of gas filtration through granular media. J Fluid Mech 2007;586:147–76.
[30] Vivek P, Sitharam TG. Shock wave attenuation by geotextile encapsulated sand barrier systems. Geotext Geomembranes 2017;45:149–60.
[31] Vivek P, Sitharam TG. Laboratory scale investigation of stress wave propagation and vibrational characteristics in sand when subjected to air-blast loading. Int J Impact Eng 2018;114:169–81.
[32] Scherbatiuk K, Rattanawangcharoen N. Experimental testing and numerical modeling of soil-filled concertainer walls. Eng Struct 2008;30:3545–54.
[33] Scherbatiuk K, Rattanawangcharoen N. A hybrid rigid body rotation model for predicting a response of a temporary soil-filled wall subjected to blast loading. Int J Impact Eng 2010;37:11–26.
[34] Omidvar M, Iskander M, Bless S. Stress-strain behavior of sand at high strain rates. Int J Impact Eng 2012;49:192–213.
[35] Radford DD, Deshpande VS, Fleck NA. The use of metal foam projectiles to simulate shock loading on a structure. Int J Impact Eng 2005;31:1152–71.
[36] Hagerty MM, Hite DR, Ullrich CR, Hagerty DJ. One-dimensional high-pressure compression of granular media. J Geotech Eng 1993;119:1–18.
[37] Han Z, Teng H, Wang J. Computer generation of sphere packing for discrete element analysis in LS-DYNA. In: 12th int LS-DYNA® users conf; 2012. p. 1–4.
[38] Uesugi M, Kishida H. Influential factors of friction between steel and dry sands. Soils Found 1986;26:33–46.
[39] Karajan N, Han Z, Teng H, Wang J. On the parameter estimation for the discrete-element method in LS-DYNA ®. 13. Th Int LS-DYNA Users Conf 2014;1–9.
[40] Jing L, Yang F, Zhao L. Perforation resistance of sandwich panels with layered gradient metallic foam cores. Compos Struct 2017;171:217–26.
[41] Lee S, Barthelat F, Hutchinson JW, Espinosa HD. Dynamic failure of metallic pyramidal truss core materials - experiments and modeling. Int J Plast 2006;22:2118–45.
[42] Maloy SA, Gray GT, Cady CM, Rutherford RW, Hixson RS. The influence of explosive-driven "Taylor-Wave" Shock prestraining on the structure/property behavior of 304 stainless steel. Metall Mater Trans A Phys Metall Mater Sci 2004;35:2617–24.
[43] Mooney M. A theory of large elastic deformation. J Appl Phys 1940;11:582–92.
[44] Rivlin RS, Trans P, Lond RS. Large elastic deformations of isotropic materials IV. further developments of the general theory. Philos Trans R Soc London Ser A, Math Phys Sci 1948;241:379–97.
[45] Pabst W, Gregorová E. Elastic properties of silica polymorphs-a review. Ceram Silokaty 2013;57:167–84.